Garcia-Donoro, D., Garcia-Castillo, L. E., Sarkar, T. K., & Zhang, Y. (2018). A Nonstandard Schwarz Domain Decomposition Method for Finite-Element Mesh Truncation of Infinite Arrays. *In IEEE Transactions on Antennas and Propagation, 66*(11), 6179–6190

DOI: 10.1109/tap.2018.2866532

Accepted version.
Published version → DOI:10.1109/TAP.2018.2866532

A Non-Standard Schwarz Domain Decomposition Method for Finite Element Mesh Truncation of Infinite Arrays

Daniel Garcia-Donoro, *Member, IEEE,* Luis E. Garcia-Castillo, *Member, IEEE,* Tapan K. Sarkar, *Fellow, IEEE,* and Zhang Yu, *Member, IEEE,*

***Abstract*—A non-standard Schwarz Domain Decomposition Method is proposed as finite element mesh truncation for the analysis of infinite arrays. The proposed methodology provides an (asymptotic) numerically exact radiation condition regardless the distance to the sources of the problem and without disturbing the original sparsity of the finite element matrices. Furthermore, it works as a multi Floquet mode (propagating and evanescent) absorbing boundary condition. Numerical results illustrating main features of the proposed methodology are shown.**

***Index Terms*—Infinite array, finite element method, mesh truncation, Schwarz domain decomposition method**

I. Introduction

THE electromagnetic analysis of periodic structures is of great importance in modern radar and communication systems. Accurate prediction of their electromagnetic behavior using numerical methods not only reduces the development cost and design timeline but also provides invaluable physical insight to design engineers.

The use of numerical methods for the electromagnetic analysis of large finite structures together with the use of higher working frequencies makes the computation, despite the constant enhancements in computer power, a challenge due to the large electrical sizes of these structures. One way to approach the electromagnetic analysis of large arrays is to solve the full problem using a pure numerical technique such as the Method of Moment (MoM) [1], [2] or the Finite Element Method (FEM) [3], [4]. It is worth to note that acceleration techniques such as the Fast Multipole Method (FMM) [5] are also widely used in the analysis of large structures. However, since these methods try to solve the full problem, their memory requirements are prohibitive and make the simulation a great challenge.

Another family of approaches make use of the infinite structure analysis, and apply post-processing techniques to correct the border effects of the structure. This type of analysis helps to understand the behavior of elements in the central region of an electrically large array, since they have similar active impedance characteristics as that of an element in an infinite array. Also, the infinite array results are used to predict the mutual coupling between the elements in an array environment or the embedded element pattern that includes mutual coupling effects. Although the infinite array results obtained do not correspond strictly speaking to a physically realistic problem, the infinite array analysis provides a reasonable good approximation with a less computing requirement than the analysis of the full problem. Furthermore, fast techniques approaches such as Macro Basis Functions or Characteristic Basis Functions [6], [7] and others use the infinite array solution as the basis brick for their approaches. Thus, the use of these infinite array solutions when analyzing electrically large antenna arrays seems an appropriate choice for fast simulations.

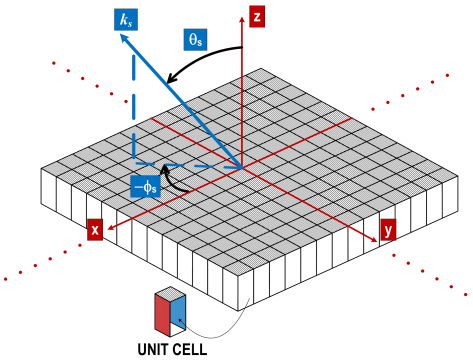

Fig. 1. Infinite periodic array in the xy-plane

In the case of antenna arrays considered in this paper, the infinite periodic structure has a two-dimensional periodicity (xy-plane). In order to truncate the computational domain along the x and y directions, a boundary condition, where the field at one face of the unit cell is related to the field at the opposite face through a simple phase shift, is considered. These boundary conditions are the so-called Periodic Boundary Conditions (PBCs) [8]. Thus, the analysis of the infinite structure is reduced to the analysis of a unit cell with PBCs assigned on the boundary surfaces of the x and y directions.

A radiation type boundary condition must be enforced on the horizontal faces to truncate the problem domain (and its discretization representation in terms of a mesh) on the z-direction. In some cases, the boundary condition associated to the horizontal face at the bottom may be different; e.g., a perfect electric conductor condition for antennas on ground plane. Figure 1 shows an example of an infinite periodic array where a unit cell is placed repeatedly in the xy-plane. The scan angle and the propagation direction, which are related to the phase shift between opposed vertical faces of the unit cell, are colored in blue.

In this paper, a non-standard Schwarz Domain Decomposition Method (DDM) is proposed as finite element mesh truncation for the analysis of infinite arrays. It shares the same approach as the mesh truncation for wave propagation open region problems called Finite Element - Iterative Integral Equation Evaluation (FE-IIEE, [9], [10]) developed by the authors and originally used in the context of hybrid methods (mainly FEM with asymptotic high frequency techniques), [11], [12]. The paper is focused on arrays but the proposed methodology is also suitable for the analysis of other infinitely periodic structures; e.g., characterization of artificial engineered materials as those composed of finite Electronic Band Gap (EBG), Photonic Band Gap (PBG), Frequency Selective Surfaces (FSS) and so on.

The proposed methodology provides an (asymptotic) numerically exact radiation condition regardless the distance to the sources of the problem and without disturbing the original sparse matrices corresponding to the FEM analysis on the unit cell.

It is worth noting that the use of Perfect Matched Layer (PML) [13] provides also theoretically (at the continuous label) an exact radiation boundary condition and is capable of absorbing multi Floquet modes. However, at the discrete level, these properties can be seriously compromised which is not the case with the non-standard Schwarz DDM truncation technique proposed in the paper.

The rest of the paper is organized as follows. The proposed methodology for mesh truncation of the unit cell is described in Section II. Numerical results of several infinite antenna arrays are shown in Section III. Benchmark tests illustrating the main features of the proposed mesh truncation technique are also shown in Section III. Finally, conclusions are given in Section IV.

II. Non-standard Schwarz DDM truncation

The non-standard Schwarz DDM truncation technique presented on this paper divides the unit cell in two overlapping domains: one finite domain (Ω^{FEM}) bounded by surface S and the infinite domain exterior to the auxiliary boundary $S^{'}$ [9], [11], [12], [14]. Thus, the overlapping region is limited by $S^{'}$ and S (see Fig. 2) The method makes use of an integral equation representation of the field exterior to $S^{'}$ obtaining the solution through an iterative process in which the residual of the radiation boundary condition on the mesh truncation boundary is updated. As in any iterative methodology, convergence is a key parameter to take into account. In the case of the proposed mesh truncation technique, convergence is assured by using convex exterior boundaries being the rate of convergence faster when the overlapping between the interior and exterior domains is larger. Studies of convergence for both 2D and 3D cases can be found in [15], [16], [9].

TABLE I
Formulation magnitudes and parameters

	$\mathbf{V}$	$\bar{\bar{f}}_r$	$\bar{\bar{g}}_r$	h	$\mathbf{O}$	$\mathbf{L}$	$\Gamma_{\mathbf{D}}$	$\Gamma_{\mathbf{N}}$
Form. $\mathbf{E}$	$\mathbf{E}$	$\bar{\bar{\mu}}_r$	$\bar{\bar{\epsilon}}_r$	η	$\mathbf{J}$	$\mathbf{M}$	Γ_{PEC}	Γ_{PMC}
Form. $\mathbf{H}$	$\mathbf{H}$	$\bar{\bar{\epsilon}}_r$	$\bar{\bar{\mu}}_r$	$\frac{1}{\eta}$	$\mathbf{M}$	$-\mathbf{J}$	Γ_{PMC}	Γ_{PEC}

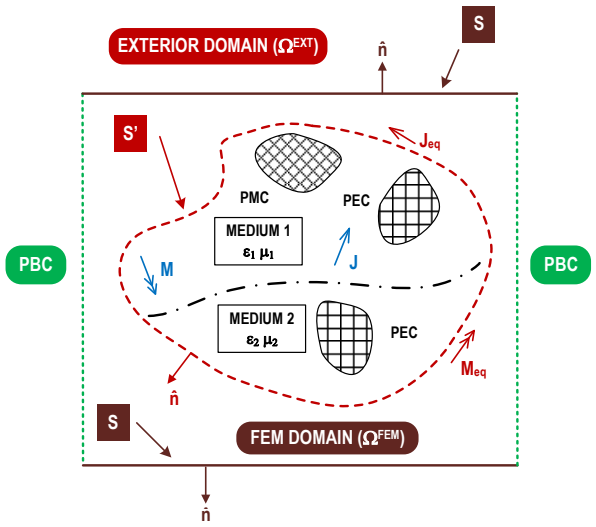

Fig. 2. Non-standard Schwarz DDM typical setup for infinite structure

The truncation method starts performing an initial FEM analysis of the unit cell using a Cauchy (Robin) boundary condition over the unbounded third non-periodic direction (labeled as S on Fig. 2). Regarding this Cauchy (Robin) boundary condition, the method supports the use of the well-known first-order absorbing boundary condition (ABC) or a modified version of the latter condition able to absorb waves out-coming from a different direction of the normal. The system of equations of this initial FEM analysis may be expressed in partitioned form as follows:

$$\begin{bmatrix} K_{II} & K_{IS} \\ K_{SI} & K_{SS} \end{bmatrix} \begin{bmatrix} g_I \\ g_S \end{bmatrix} = \begin{bmatrix} b_I \\ b_\Psi \end{bmatrix} \tag{1}$$

where the sub-indexes S and I refer to the degrees of freedom g associated to the surface S and those associated to nodes in the interior of S, respectively.

$$K = \underbrace{\int_\Omega \boldsymbol{\nabla}\times\mathbf{F}\cdot\left(\bar{\bar{f}}_r^{\,-1}\boldsymbol{\nabla}\times\mathbf{V}\right)dv - k_0^2\int_\Omega \mathbf{F}\,\bar{\bar{g}}_r\,\mathbf{V}dv}_{K_{II},K_{SI},K_{IS}} + \underbrace{\gamma\iint_{\Gamma_C}(\hat{\mathbf{n}}\times\mathbf{F})\cdot(\hat{\mathbf{n}}\times\mathbf{V})\,dS}_{K_{SS}} \tag{2}$$

$$b = \underbrace{\int_\Omega \mathbf{F}\cdot\mathbf{q}\,dv}_{b_I} - \underbrace{\int_{\Gamma_C}\mathbf{F}\cdot\boldsymbol{\Psi}\,dS}_{b_\Psi} \tag{3}$$

$$\mathbf{q} = -j\,k_0\,\eta_0\,\mathbf{O} - \boldsymbol{\nabla}\times\left(\bar{\bar{f}}_r^{\,-1}\mathbf{L}\right) \tag{4}$$

with

$$\mathbf{F} := \{\mathbf{A}\in\mathbf{H}(\text{curl},\Omega), \hat{\mathbf{n}}\times\mathbf{A} = 0 \quad \text{on } \Gamma_D\} \tag{5}$$

and $\mathbf{H}$(curl) being the space of square integrable vector functions with square integrable curl. Further details can be found in [17].

The discretization of the above variational formulation is achieved by using our own versions of higher-order isoparametric curl-conforming basis functions that constitute a rigorous implementation of Nédélec first family of finite elements [18]. Specifically, second order basis functions are used in this case. It is important to remark that the basis functions are obtained in the reference finite element and then, transformed to the real one using the inverse of the Jacobian matrix. The reader may refer to [19]–[21].

The right hand side term $\{b_I\}$ corresponds to the interior current sources $\mathbf{J}$ and $\mathbf{M}$ and the inward waves impressed at the ports. The term $\{b_\Psi\}$ is related to the residual $\mathbf{\Psi}$ of the boundary condition at the truncating boundary S; that is, the first-order ABC or its modified version. In order to help the reader to understand the iterative process described next, the expression of the first-order ABC is introduced now, which is particularized for the upper truncation surface of a unit cell

$$\hat{\mathbf{z}} \times \left(\bar{\bar{f}}_r^{\,-1} \boldsymbol{\nabla} \times \mathbf{V} \right) + j\, k\, (\hat{\mathbf{z}} \times \hat{\mathbf{z}} \times \mathbf{V}) = \mathbf{\Psi} \tag{6}$$

where k typically is the vacuum wavenumber. The value of $\mathbf{\Psi}$ in (3) is the result of evaluating the first two terms of the previous equation with $\mathbf{V} = \mathbf{V}^{\text{inc}}$ being $\mathbf{V}^{\text{inc}}$ the incident electric/magnetic field (see table I for details about the magnitudes involved in the calculation).

Once the system of equations is obtained, the iterative process in which the residual of the radiation boundary condition is updated begins. This process is summarized next:

- **Step 1:** An initial value of $\mathbf{\Psi}$, denoted as $\mathbf{\Psi}^0$, is assumed. Specifically, $\mathbf{\Psi}^0$ is zero for radiation problems and $\mathbf{\Psi}^0 = \mathbf{\Psi}^{\text{inc}}$ for scattering problems. Then, the initial right hand side term b_Ψ^0 is obtained.
- **Step 2:** The FEM system of equations (1) is now solved. After that, electric and magnetic fields on $S^{'}$ are calculated in order to compute the corresponding current densities $\mathbf{J}_{\text{eq}}$ and $\mathbf{M}_{\text{eq}}$ of the equivalent exterior problem.
- **Step 3:** The scattering field, and its curl, over S radiated by the equivalent currents $\mathbf{J}_{\text{eq}}$ and $\mathbf{M}_{\text{eq}}$ are calculated. The fields radiated by the FEM region, $\mathbf{V}_{\text{FE-IIEE}}$ and their curl $(\boldsymbol{\nabla} \times \mathbf{V})_{\text{FE-IIEE}}$, are computed using the integral expressions

$$\begin{aligned} \mathbf{V}_{\text{FE-IIEE}} = & \oiint_{S'} \left(\mathbf{L}_{\text{eq}} \times \boldsymbol{\nabla}\, G_p \right)\, dS' \\ & - jkh \oiint_{S'} \left[\mathbf{O}_{\text{eq}} \left(G_p + \frac{1}{k^2}\, \boldsymbol{\nabla}\, \boldsymbol{\nabla}\, G_p \right) \right] dS' \end{aligned} \tag{7}$$

$$\begin{aligned} (\boldsymbol{\nabla} \times \mathbf{V})_{\text{FE-IIEE}} = & jkh \oiint_{S'} \left(\mathbf{O}_{\text{eq}} \times \boldsymbol{\nabla}\, G_p \right)\, dS' \\ & - \oiint_{S'} \left[\mathbf{L}_{\text{eq}} \left(k^2\, G_p + \boldsymbol{\nabla}\, \boldsymbol{\nabla}\, G_p \right) \right] dS' \end{aligned} \tag{8}$$

where h is the immittance of the homogeneous medium (see table I), and G_p denotes the periodic Green's function for a homogeneous medium. It is worth mentioning that an accurate and efficient evaluation of the periodic Green's function is of fundamental importance for the analysis of structures using the previous integral equations. Details about the periodic Green's function and its convergence rate are given in a later subsection.

- **Step 4:** A new value of $\mathbf{\Psi}$, ($\mathbf{\Psi}^{i+1}$ in general) is computed by introducing the values of the fields $\mathbf{V}_{\text{FE-IIEE}}$ and $(\boldsymbol{\nabla} \times \mathbf{V})_{\text{FE-IIEE}}$ in equation (6) where i means the iteration number.
- **Step 5:** The error between $\mathbf{\Psi}^{i+1}$ and $\mathbf{\Psi}^i$ is calculated. If the error is greater than an error threshold, the method will start again for step 2 (using $\mathbf{\Psi}^{i+1}$ as the new residual function); otherwise the iteration process finishes. The error in $\mathbf{\Psi}$ is measured in a weighted L_2-norm

$$\text{error}_i = \frac{\left\| \mathbf{\Psi}^i - \mathbf{\Psi}^{i-1} \right\|_2}{\left\| \mathbf{\Psi}^i \right\|_2} \tag{9}$$

Thus, a (numerically) exact radiation boundary condition is imposed absorbing any out-coming wave avoiding that undesired reflexions come back to the computational domain. The proposed numerical technique also allows the external boundary to be placed close to the sources, while the sparsity of the FEM matrices is retained. It is worth noting that the numerical cost of the second and subsequent iterations is very small since the factorization of the FEM matrix must be performed only once at the first iteration (if direct solvers are used).

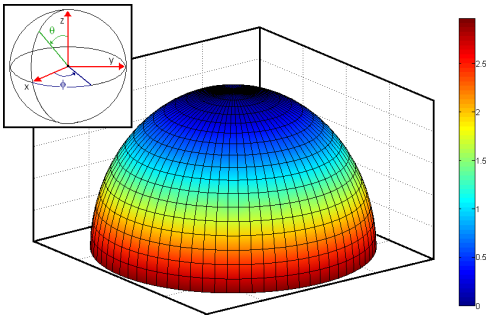

Fig. 3. Standard first-order absorbing boundary condition values for waves propagating in different (θ_s, ϕ_s) directions

A. Standard first-order absorbing boundary condition

As aforementioned, one of the Cauchy (Robin) boundary condition supported by the proposed truncation method is the well-known first-order ABC. The implementation of this boundary condition in a finite element formulation is straightforward. However, as it is well-known, this condition is only satisfied for waves propagating along the z-direction (i.e., only absorbs waves propagating along $\theta_s = 0$), and it has a significant reflection for waves propagating in other directions. Thus, this reflection may produce disturbances when analyzing infinite periodic structures in which the solution contains significant wave components traveling in other directions different from the z-direction.

Figure 3 shows the residual of equation (6) for waves propagating along different directions ranging from $0° \leq \phi_s \leq 360°$ and from $0° \leq \theta_s \leq 90°$. The incident frequency is 100 MHz and $(0, 0, 1)$ is the observation point where equation (6) is evaluated.

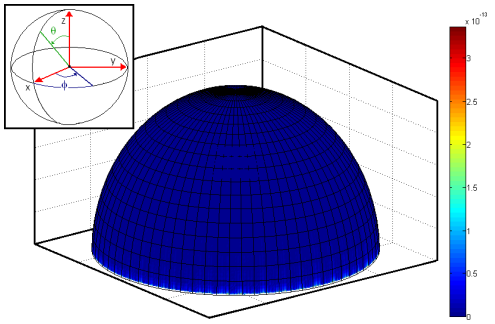

Fig. 4. Modified first-order absorbing boundary condition values for waves propagating in different (θ_s, ϕ_s) directions

The figure shows clearly how the condition absorbs the waves propagating along the z-direction (values in blue in the figure) and how, as the angle θ_s increases, the condition does not absorb the incident waves (values changing from blue to red in the figure). Thus, when using this boundary condition over the surface S and the propagating direction of the array is different the initial solution will contain reflections that has to be canceled with the proposed iterative truncation method. In this case, the number of iterations required by the truncation method is high since the standard ABC is not helping to absorb any initial out-coming wave. A numerical experiment proving this behavior is illustrated in the numerical result section.

B. Modified first-order absorbing boundary condition

Another boundary condition supported by our non-standard Schwarz DDM truncation technique is a modified ABC that can absorb plane waves propagating in any (θ_s, ϕ_s) direction. Following the procedure described in [3, Section 9.1.2], the expression of this modified first-order ABC is given by

$$\hat{\mathbf{z}} \times \left(\bar{\bar{f}}_r^{\,-1} \boldsymbol{\nabla} \times \mathbf{V} \right) + j\, k \cos\theta_s \left(\hat{\mathbf{z}} \times \hat{\mathbf{z}} \times \mathbf{V} \right) - \frac{jk}{\cos\theta_s} \mathbf{k}_t^s \left(\mathbf{k}_t^s \cdot \mathbf{V} \right) - \boldsymbol{\Psi}^{\mathbf{inc}}_{\theta_s, \phi_s} = 0 \quad (10)$$

where k typically is the vacuum wavenumber, $\mathbf{k}_t^s = \sin\theta_s \cos\phi_s\, \hat{x} + \sin\theta_s \sin\phi_s\, \hat{y}$ with (θ_s, ϕ_s) being the scan angles of the array and $\boldsymbol{\Psi}^{\mathbf{inc}}_{\theta_s, \phi_s}$ is the result of evaluating the first three terms of equation (10) with $\mathbf{V} = \mathbf{V}^{\text{inc}}$ being $\mathbf{V}^{\text{inc}}$ the incident electric/magnetic field.

Figure 4 shows the residual of equation (10) for the waves propagating in the same directions than the previous figure. The frequency of the plane waves and the observation point where the equation is evaluated are also the same than the previous case. The figure shows how the modified condition absorbs perfectly any plane wave propagating in the (θ_s, ϕ_s) direction (except waves propagating along $\theta_s = 90°$ where a indetermination in one term of the equation is found). However, it is worth to note that, although being able to absorb perfectly any plane wave propagating in the (θ_s, ϕ_s) direction, this modified ABC is not able to absorb two different plane waves (or Floquet modes) propagating in two different (θ_s, ϕ_s) directions at the same time.

When using this boundary condition over the surface S and the propagating direction (θ_s, ϕ_s) of the array is selected to be absorbed, the initial solution will contain small reflections (or even none). Thus, only one or two iterations are required by the truncation method to absorb all the out-coming waves. A numerical experiment proving this behavior is also illustrated in the numerical result section.

C. Periodic Green's Function

As commented in the step 3 of the iterative truncation algorithm, the periodic Green's function for an homogeneous medium is used to calculate the radiated fields over the external boundary S (first and second derivatives are also required). First of all, let us assume a periodic structure in the xy-plane as the one shown in Fig. 1. The (m, n) cell of the structure is obtained by shifting the $(0, 0)$ cell through the relation

$$\rho_{mn} = m\, \mathrm{D_x}\, \hat{x} + n\, \mathrm{D_y}\, \hat{y} \quad (11)$$

where $\mathrm{D_x}$ and $\mathrm{D_y}$ are the periodic distances in the x- and y-directions. Thus, the periodic Green's function $G_p(\mathbf{r}, \mathbf{r}_s)$ in the spatial domain has the form

$$G_p\left(\mathbf{r}, \mathbf{r}_s\right) = \sum_{m=-\infty}^{\infty} \sum_{n=-\infty}^{\infty} e^{-j(k_x m \mathrm{D_x} + k_y n \mathrm{D_y})} \frac{e^{-jk_0 R_{mn}}}{4\pi R_{mn}} \quad (12)$$

where

$$k_x = k_0 \sin\theta_s \cos\phi_s \qquad k_y = k_0 \sin\theta_s \sin\phi_s \quad (13)$$

with θ_s and ϕ_s as the scan angles that determinate the phase-shift between the different adjacent cells and R_{mn} is the distance between the source in the corresponding cell and the observation point.

The main constraint of these series is their slow convergence rate for the free space case. Equation (12) is extremely slow to converge (for arbitrary d, the number of terms having magnitude 10^{-d} is of order 10^{+2d}) making the numerical evaluation of the series difficult and computationally expensive.

Many techniques exist for accelerating slowly-convergent series such as the Euler Transformation [22, Equation 3.6.27], the Shank Transformation [23], the Poisson Transformation, the Ewald Transformation [24], [25] or the Kummer Transformation [22, Equation 13.1.27]. A survey of them and their use in evaluating periodic sums of three-dimensional points sources is given in [26]. Among these techniques, the one chosen to accelerate the series in the present paper has been the Ewald's transformation. This transformation has been considered in the literature as the reference method for the efficient numerical calculation of the periodic Green's function. Details about our implementation of the Ewald's transformation can be found on [27], [28].

D. Convergence

As iterative methodology, the convergence of the method is a key parameter to take into account. The convergence of the proposed non-standard Schwarz DDM truncation method is assured in the case of a sphere (circle in 2D) is used as truncation boundary of "large enough" radius [15], [16]. It is shown empirically that convergence is obtained for any arbitrary convex truncation boundary [9]. It is worth noting

that previous works make use of the conventional free space Green's function in order to calculate the scattering fields required in the truncation. However, the proposed methodology makes uses of the periodic Green's function when truncating the non-periodic direction in the unit cell. This difference produces changes in the convergence properties of the solver that are included in the numerical results confirming empirically the above claims.

III. Numerical results

To illustrate the capabilities of the proposed non-standard Schwarz DDM truncation technique five different examples have been analyzed. The first example has consisted on the analysis of an infinite ground plane. It is worth mentioning that this example may be used as validation test since the result of this analysis may be compared with an analytic solution. The second example has consisted of the analysis of a microstrip patch phased array. The results of this analysis have been compared with those given by the MoM simulation for both 11 x 11 and 22 x 22 finite arrays. The third example has consisted of the analysis of a cross-shaped frequency selective surface (FSS) using three different configurations; 6 x 6, 12 x 12 and 24 x 24 elements. In the fourth example, the broadside analysis of a multilayer aperture antenna has been carried out. The results using the infinite approach have been compared with those given by the finite analysis of an 8 x 8 array. Finally, the last example has consisted of the analysis of an infinite phased array based on Vivaldi antennas. The analysis has been performed for both broadside and oblique scan angles.

A. Analysis of infinite ground plane

This first example has consisted on the analysis of an infinite ground plane illuminated by a plane wave under different angles (normal and oblique incidence). As aforementioned, the accuracy and the capabilities of the proposed truncation technique have been checked comparing the results with an analytic solution.

1) Normal incidence: In this first test, the infinite ground plane has been illuminated by a plane wave with $\phi = 0^\circ$ and $\theta = 0^\circ$ as incident angles. The plane wave has been polarized in both ϕ- and θ-components and the working frequency has been set to 300 MHz. The unit cell considered for this test has been an hexahedron with 0.25 m long by 0.25 m wide by 0.5 m high. The ground plane has been placed in the xy-plane. Note that the solution to this problem is a standing wave (SW) with a wavelength of 0.5 m. Thus, it is easy to see if the results given by the analysis are correct, since a complete period of the SW should be appreciated along the z-axis of the unit cell. Figure 5 shows the unit cell model used in this test.

A first-order ABC has been assigned over the surface S in the non-periodic direction (z-axis) . The expression of the modified ABC for the scan angle $\theta_s = 0^\circ$ matches with the first-order ABC. Thereby, only the conventional ABC has been used over the surface S during this analysis. Figure 6 shows the magnitude of the E-field ($|\mathbf{E}|$) after the first iteration of the proposed iterative truncation method is completed. As expected, a complete period of the standing

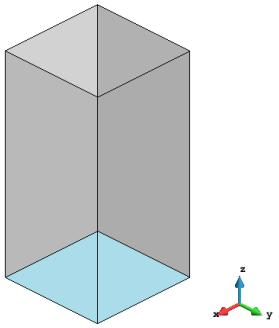

Fig. 5. Unit cell model for infinite ground plane

wave is appreciated, since the ABC condition is able to absorb completely the initial out-coming wave with no reflection. The number of iterations employed by the iterative truncation method was one, obtaining in this iteration a relative error of $5.23 \cdot 10^{-8}$. Therefore, this first test confirms the expected behavior of the truncation method when using a first-order ABC and the waves are out-coming in the normal direction.

2) Oblique incidence: In this case, the infinite ground plane has been illuminated by a plane wave coming from $\phi = 20^\circ$ and $\theta = 60^\circ$. The plane wave has been polarized in the ϕ-component and the working frequency has been set to 300 MHz. The unit cell considered for this test has been the same than the previous example. The solution to this problem is another SW but with a wavelength of 1.0 m, instead of 0.5 m. Thus, a half period of the SW should be appreciated along the z-axis of the unit cell.

The first boundary condition considered is the modified ABC. Figure 7 shows the magnitude of the E-field after the first iteration of the truncation process is completed. As expected (concluded from the previous test), if the boundary condition over the surface S can absorb completely the initial out-coming wave with no reflection, the iterative truncation method needs just one iteration to obtain a numerical exact radiation boundary condition (relative error of $1.09 \cdot 10^{-8}$ in this case).

However, if the original first-order ABC is used over the surface S, the absorbing condition is not satisfied for the plane wave used in this example ($\phi = 20^\circ$ and $\theta = 60^\circ$) and significant reflections appear. Figure 8(a) shows the magnitude of the E-field after the first iteration is completed, where a substantial

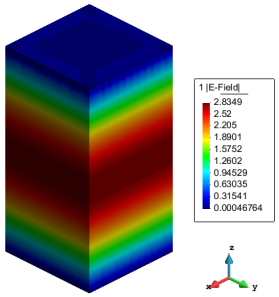

Fig. 6. $|\mathbf{E}|$ after first iteration for normal incidence.

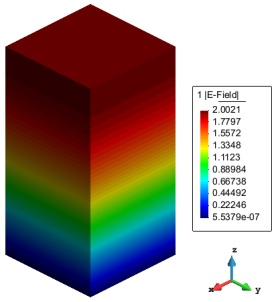

Fig. 7. $|\mathbf{E}|$ after first iteration for oblique incidence using the modified ABC as absorbing boundary condition.

reduction on the maximum of the SW is appreciated due to the reflection produced in the truncation boundary. In this case, the iterative truncation method continues updating the radiation boundary condition and it is able to cancel all the undesired reflexions up to an arbitrary low predetermined relative error. Considering a relative error of 10^{-8}, the truncation method reaches the solution after 14 iterations. Figure 8(b) shows the magnitude of the E-field after 14 iterations. Comparing this result with the SW illustrated on Fig. 7, one can see how the iterative truncation method reaches the same solution.

Figure 9 shows the convergence rate of the truncation method for this oblique incidence case. The number of iterations extends to 40 in order to check when the truncation method using the conventional ABC provides the same residual error than using the modified ABC. Typically, one can consider residual errors below 10^{-6} a numerically exact radiation condition. As aforementioned, the iterative truncation method provides residual errors below 10^{-8} from the first iteration using the modified ABC. In the case of the conventional ABC, the iterative truncation method requires 14 iteration to reach the same residual error than the first iteration of the modified ABC (marked in green in the figure). This example demonstrates that, even when the initial FEM simulation presents undesired reflections, the iterative truncation method presented in this paper is able to absorb them no matter the absorbing boundary condition employed on the external boundary.

As mentioned in the previous section, the use of the periodic Green's function in the proposed truncation method changes the convergence properties of the method with respect to the

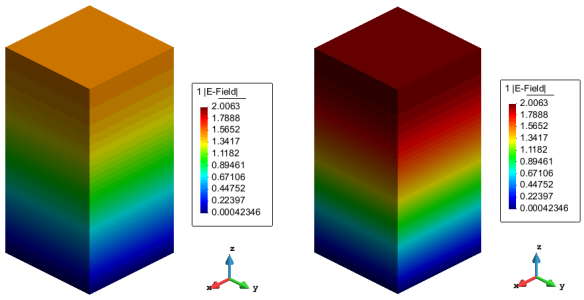

(a) after first iteration (b) after 14 iterations

Fig. 8. Comparison of the $|\mathbf{E}|$ for the second test

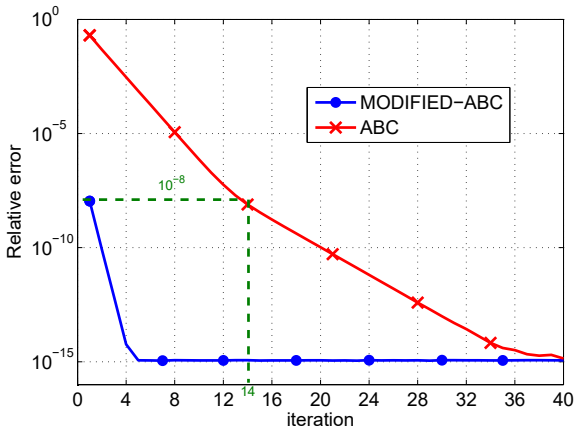

Fig. 9. Convergence plot of the iterative method for oblique case

case of using the conventional free space Green's function. In order to investigate this issue, the simulation of a finite ground plane is carried out increasing its dimensions each time. In this way, as the finite ground plane increases, the behavior of the free space Green's function tends to be similar to the periodic Green's function. Figure 10 shows again the magnitude of the E-field (in the center of the plane with the same dimensions as the unit cell) when the side of the finite ground plane goes from 0.75 meters to 5 meters long. One can see how, as the size of the finite plane increases, the half period of the standing wave appears more clearly confirming the correctness of the solution.

Figure 11 shows the comparison of the convergence rate of the truncation method using the periodic Green's function (blue line) versus the free space Green's function for three different finite sizes of the ground plane, specifically of side

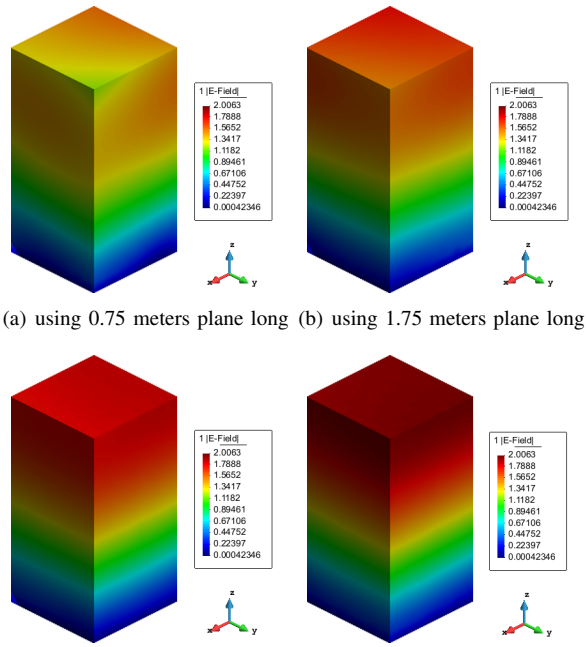

(a) using 0.75 meters plane long (b) using 1.75 meters plane long

(c) using 3.25 meters plane long (d) using 5 meters plane long

Fig. 10. Comparison of the $|\mathbf{E}|$ for finite ground plane with different sizes

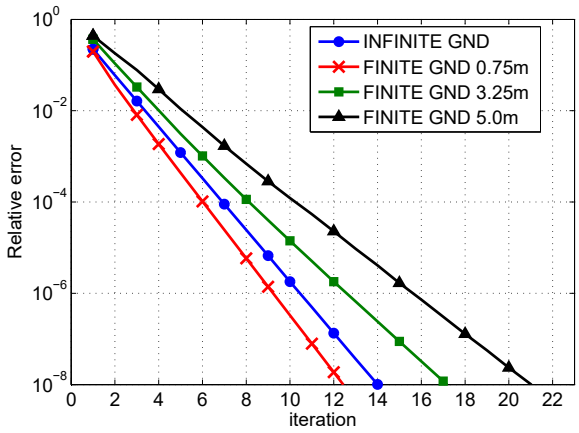

Fig. 11. Comparison of the convergence rate for different Green's functions in the oblique case

lengths equal to 0.75, 3.25 and 5.0 meters. As the size of the finite plane increases, the number of elements employed in the calculation of the scattering field is larger, tending to the values given by the periodic Green's function. However, the convergence rate when incresing the finite ground plane is getting slower than the one given by the infinite approach (using periodic Green's function). Thus, the proposed truncation method presents a faster convergence rate than the original truncation method that employs the free space Green's function.

B. Microstrip patch phased array

A microstrip patch phased array has been analyzed in this example using the infinite array approach proposed in the paper. The array is printed on a substrate $\epsilon_r = 2.67$ and is housed in a 520 mm x 580 mm x 7 mm cavity in a ground plane [29] as illustrated in Fig. 12. The dimensions of each patch element are 30 mm x 35.6 mm and the gaps between any two neighbor elements are 14 mm along both length and width directions.

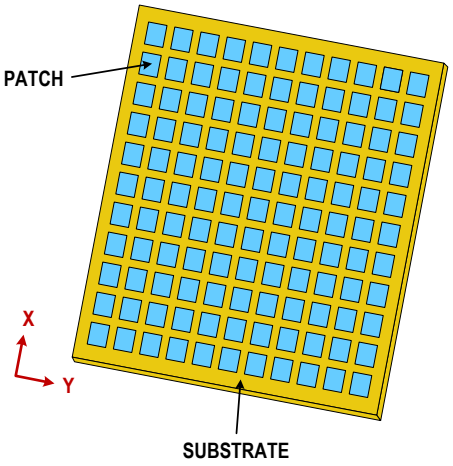

Fig. 12. Perspective view of the 11 x 11 microstrip patch array

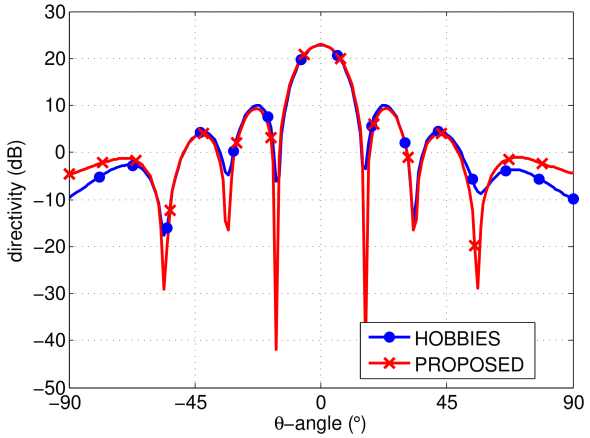

(a) Comparison for 11 x 11 array

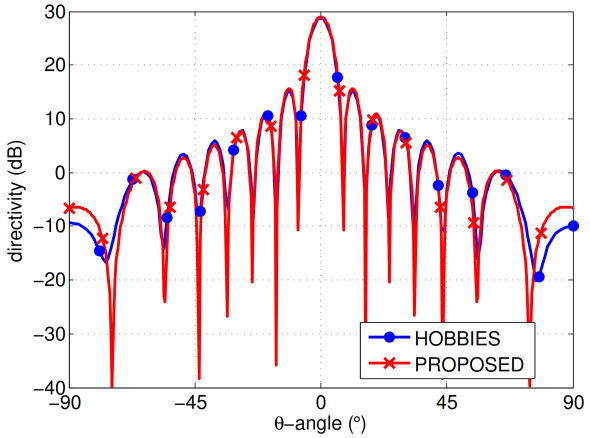

(b) Comparison for 22 x 22 array

Fig. 13. Comparison of radiation pattern cut ($\phi = 90°$) for microstrip array

Once the electromagnetic field in the unit cell is obtained (and hence currents on the unit cell boundaries) the radiated field of a finite array using a given number of elements as those of the unit cell may be obtained by simply multiplying the radiated field of the unit cell by the array factor. The radiation patters so obtained are shown in Fig. 13 for two configurations: 11 x 11 and 22 x 22. The FEM results obtained in this test have been compared with the ones given by the commercial software HOBBIES [30] that is based on MoM.

HOBBIES has been used to analyze the whole arrays directly without using any approximation technique. The distance between elements used in the FEM analysis has been set to 0.37λ. Figure 13 shows the comparison of a radiation pattern cut ($\phi = 90°$) for both configurations. The results present a very good agreement for all the angles except for those close to grazing angles to the structure ($|\theta| \geq 75°$) where the border-effect is most relevant. It is worth noting that, as the number of elements of the finite array increases, the discordant angles are closer to $\theta = \pm 90°$ as it is observed by comparison of Fig.13(a) and Fig.13(b).

C. Cross-shaped Frequency Selective Surface

The next example consists of the analysis of a cross-shaped FSS printed on a layer of thin dielectric substrate. As the

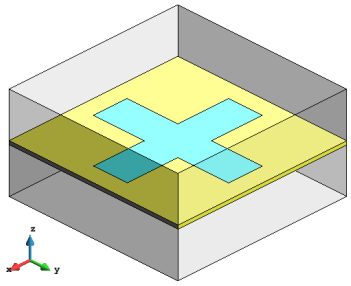

Fig. 14. Perspective view of the cross-shaped FSS unit cell

previous example, the FEM results obtained using the infinite approach have been compared with the results obtained by analyzing the whole finite structure with HOBBIES. Three different array configurations in terms of number of cells have been considered (6 x 6, 12 x 12 and 24 x 24). Thus, the border-effect can also be investigated in this case.

The FSS consists of a cross-shaped metal patch array printed on a layer of thin dielectric substrate [31] ($\varepsilon = 4.0$ and $h = 1$ mm). The unit cell of the FSS has a length of 50 mm by 50 mm where the dimensions of one arm of the cross are 10 mm by 15 mm. The absorbing boundary condition is placed at 0.125 λ from the structure. Figure 14 illustrates the geometry of the unit cell of the FSS. This structure is illuminated by an incident plane wave at 3.0 GHz in the broadside direction $(\phi = 0°, \theta = 0°)$.

Figure 15 shows the comparison of a scattering cut $(\phi = 90°)$ where again a very good agreement is appreciated except for those angles where the border-effect is more relevant. As the number of elements of the finite FSS increases, the starting discordant angle moves to angles closer to $\theta = \pm 90°$. In this particular case from $\theta = \pm 30°$ (Fig. 15(a)) to $\theta = \pm 45°$ (Fig. 15(c)). Thus, this demonstrates that the difference in the results is due to approximating a finite structure with an infinite approach.

The convergence of the iterative method for this example is shown in Fig. 16. The convergence rate depends on the distance between the structure and the absorbing boundary condition. The figure shows the convergence rate using three different distance (0.4 λ, 0.25 λ and 0.125 λ). In this way, the convergence rate of the method is also investigated concluding that the convergence behavior with the use of the periodic Green's function is qualitatively the same than with the free space Green's function. Nevertheless, as it was shown in Section III-A2, the convergence with the infinite approach is faster than when analyzing the equivalent whole finite structure as the electrical size of the problem domain under analysis is much smaller.

D. Multilayer aperture coupled antenna

In this fourth example, the infinite analysis of a 8 x 8 multilayer aperture coupled antenna array is carried out. The antenna elements work at 4 GHz and are placed periodically along the xy-plane with a distance between elements of 0.6 λ.

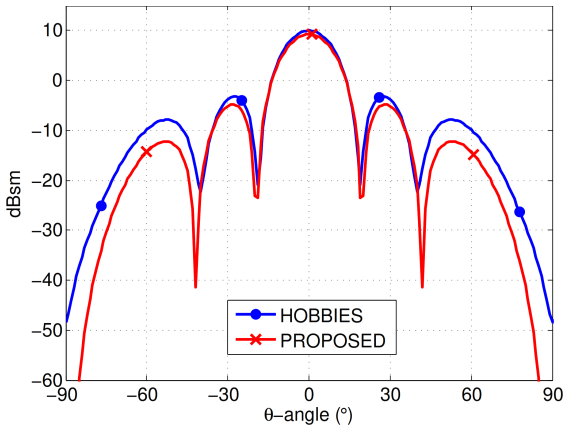

(a) Comparison for 6 x 6 FSS array

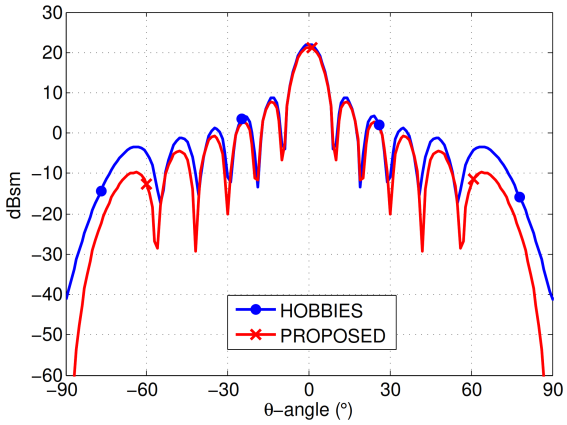

(b) Comparison for 12 x 12 FSS array

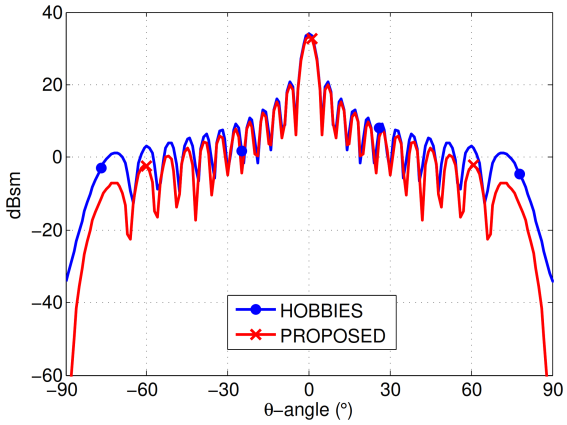

(c) Comparison for 24 x 24 FSS array

Fig. 15. Comparison of scattering cut $(\phi = 90°)$ for cross-shaped FSS array

Their design was taken from the antenna elements published in [32]. Figure 17 shows the different views for the three layers that form the antenna; director, driver and reflector layer. The dimensions of the elements of the antenna are marked in the figure. Both driver and director layers are printed on a substrate with $\varepsilon_r = 2.2$ and $h = 0.524$ mm.

Figure 18 shows the comparison of a radiation pattern cut $(\phi = 0°)$ where, as in the previous examples, a very good agreement is appreciated except for grazing observation angles where the border-effect is more relevant.

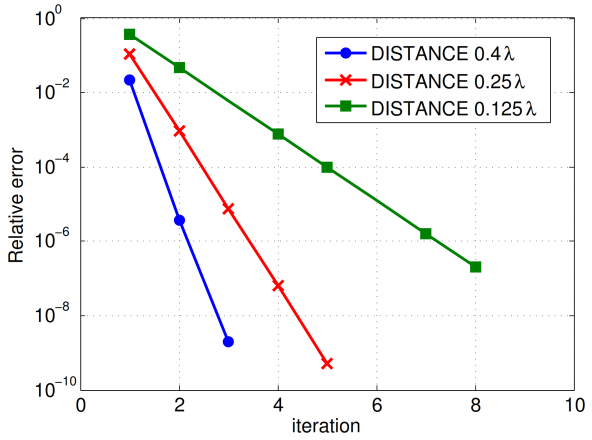

Fig. 16. Convergence plot of the iterative method for cross-shaped FSS

The convergence of the iterative method for different distances between the structure and the absorbing boundary condition is shown Fig. 19. As previous cases, shorter distances produce larger convergence rates.

E. Vivaldi antenna phased array

A phased antenna array based on a Vivaldi element, as the one shown in Fig. 20, is considered in this example [3]. A dielectric substrate ($\varepsilon_r = 6$) with a conducting surface on one side is positioned normal to the ground plane. The dimensions of the unit cell are T_x = 36 mm and T_y = 34 mm, and the height of the substrate is 33.3 mm with a thickness of 1.27 mm. The coaxial waveguide is empty with the radii of the inner and outer conductors equal to 0.375 and 0.875 mm, respectively.

The results obtained with the proposed truncation technique has been compared in this case with the commercial software HFSS [33]. The particularity of this example resides on the sharp peak occurring at 4.6 GHz when the array is configured for broadside radiation. The peak is reported in the literature to be caused by mutual coupling between antenna elements due to presence of surface waves on the dielectric. As a result, there

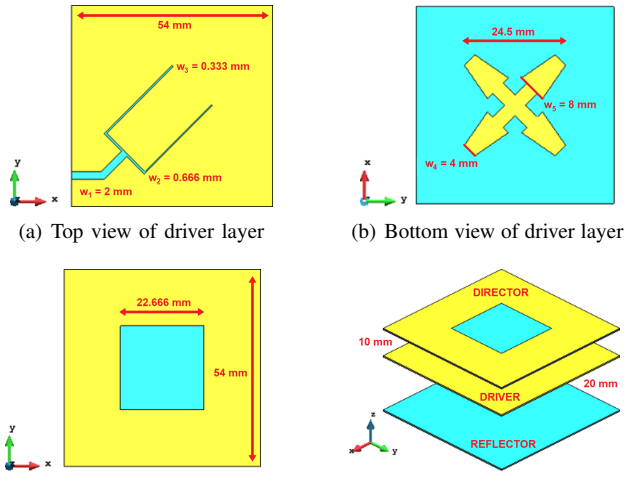

(a) Top view of driver layer (b) Bottom view of driver layer

(c) Top view of director layer (d) 3D view of antenna element

Fig. 17. Multilayer aperture couple antenna unit cell

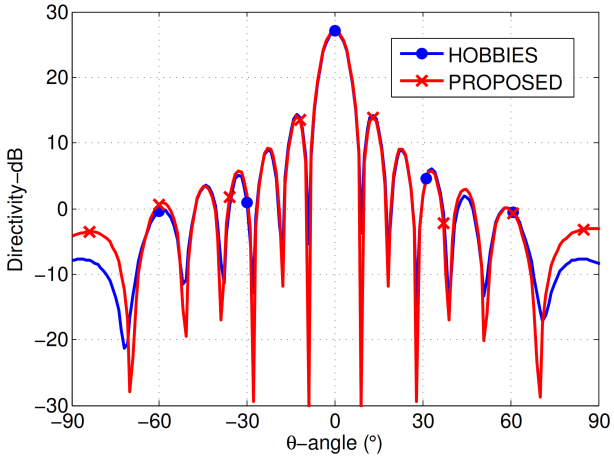

Fig. 18. Comparison of radiation pattern cut ($\phi = 0°$) for 8 x 8 aperture coupled antenna array

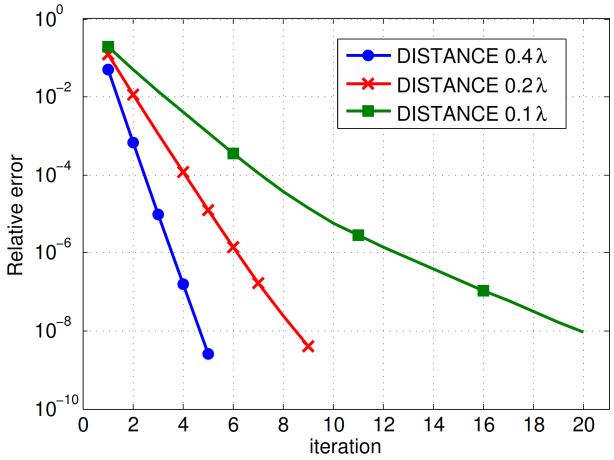

Fig. 19. Convergence plot of the iterative method for aperture antenna array

is a situation of "scan blindness" in the array at that particular frequency and scan angle. Figure 21 shows the results of the reflexion coefficient (S_{11}) for the broadside scanning ($\phi_s = 0°, \theta_s = 0°$) and the oblique scanning ($\phi_s = 135°, \theta_s = 45°$) where a good agreement is appreciated between both FEM analysis. As the figure shows, our FEM analysis catches the mentioned sharp peak perfectly indicating the infinite approach simulation is correct and, in consequent, the mesh truncation technique is successfully implemented.

This structure and the correct capture of its "scan blindness" effect is used next to illustrate one the features of the proposed methodology with respect to a conventional ABC. Consider Fig. 22 in which the reflection coefficient (S_{11}) for the broadside scanning ($\phi_s = 0°, \theta_s = 0°$) is shown again as in Fig. 21(a). The figure shows the magnitude of S_{11} when an ABC is used to truncate the problem at a distance from the antenna equal to $0.5\,\lambda$ and equal to $0.1\,\lambda$. It is very clear that conventional ABC simply does not work for the $0.1\,\lambda$ case and it does require a distance equal to $0.5\,\lambda$ in order to capture the blindness effect. In contrast, the proposed methodology works with a distance equal to $0.1\,\lambda$. Actually, it works even with shorter distances; it is just a matter of a

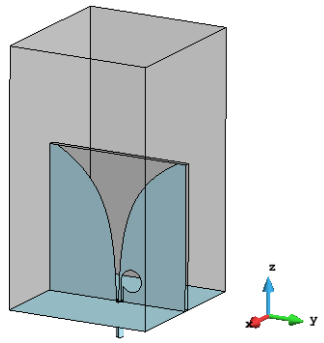

Fig. 20. Unit cell of an infinite phased array of Vivaldi antennas where the distance to the truncation surface is $d = 0.5\lambda$

few extra iterations of the method. Thus, the reliability and level of accuracy of the results obtained with the proposed methodology is assured, even in the case the user does not set up the truncation boundary far enough for the specific structure under analysis and level of accuracy demanded.

Fig. 23 shows the convergence of the iterative method when the problem is truncated at a distance of $0.5\,\lambda$, $0.3\,\lambda$ and $0.1\,\lambda$. It is worth noting that the aforementioned behavior may be appreciate, where shorter distances, although produce smaller problem sizes, imply higher number of iterations of the method.

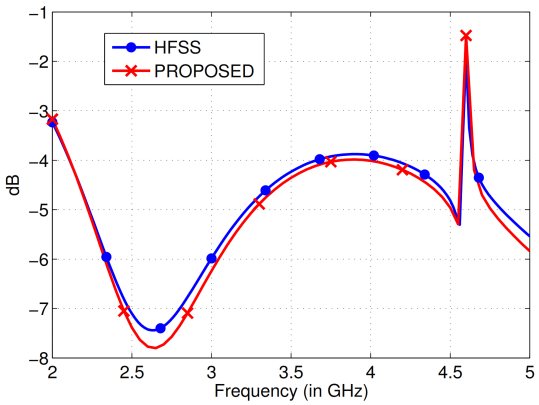

(a) Broadside scanning $(\phi_s = 0°, \theta_s = 0°)$

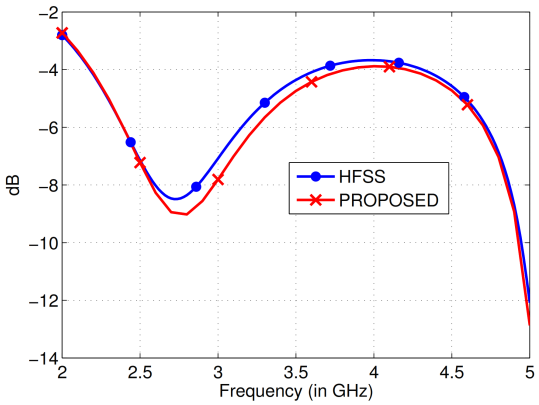

(b) Oblique scanning $(\phi_s = 135°, \theta_s = 45°)$

Fig. 21. Comparison of $|S_{11}|$ parameter for a Vivaldi phased array

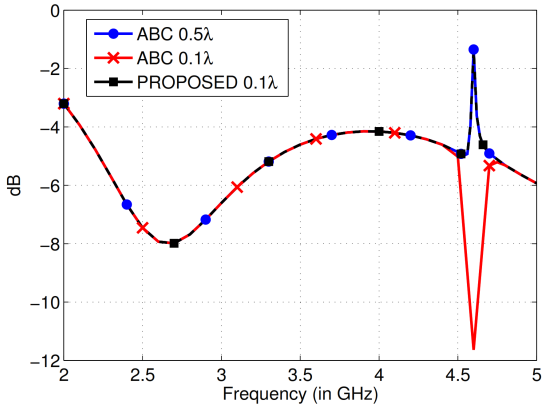

Fig. 22. Effect of the distance of the mesh truncation boundary with conventional ABC and the proposed methodology on the magnitude of S_{11} parameter for the Vivaldi phased array under broadside situation $(\phi_s = 0°, \theta_s = 0°)$.

Finally, a comparison on the computational time between HFSS and the proposed method for one frequency simulation (4.6 GHz) is given. The benchmark is performed on a desktop computer with an Intel(R) Core(TM) i7-4790 CPU @ 3.60 GHz and 16.0 GB of RAM. The problem is truncated at 0.5λ in both cases. The mesh size in both softwares is fixed to be 0.05λ obtaining a final mesh of 35,409 tetrahedron for HFSS and 31,500 elements for our FEM. The total time employed by HFSS in this simulation is 45 seconds (only counting the simulation time of the last adaptive step with 35,409 tetrahedron), while the total time used by the proposed technique is 51 seconds. As one can see, the proposed technique is little bit slower than HFSS, however HFSS required 1.93 GB of memory to perform the simulation meanwhile the proposed technique only requires 1.6 GB. It is worth noting that, using the proposed truncation technique, the external boundary can be placed at 0.1λ reducing the finite elements in the mesh up to 20,432. This implies a reduction in the memory used in the simulation (requiring now only 1.02 GB), but an increment in the computational time due to the higher number of iterations of the method (121 seconds). Thus, it is proof that the performance of the proposed mesh truncation technique are competitive in comparison with commercial softwares like HFSS.

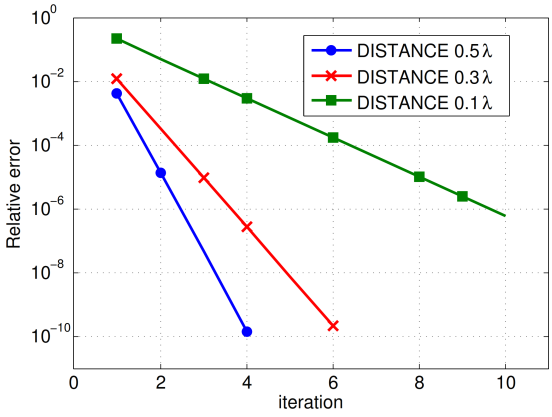

Fig. 23. Convergence of the iterative method for Vivaldi phased array

IV. Conclusion

A non-standard Schwarz Domain Decomposition Method truncation technique for the analysis of infinite arrays has been presented. The proposed methodology provides an (asymptotic) numerically exact radiation condition regardless the distance to the sources of the problem and without disturbing the original sparse matrices corresponding to the FEM analysis on the unit cell. The paper is focused on arrays but the proposed methodology is also suitable for the analysis of other infinitely periodic structures; e.g., characterization of artificial engineered materials as those composed of finite Electronic Band Gap (EBG), Photonic Band Gap (PBG), Frequency Selective Surfaces (FSS) and so on. Numerical examples have demonstrated the performance and capabilities of the proposed truncation method when analyzing antenna arrays. The reliability and level of accuracy of the results obtained with the proposed methodology is assured, even in the case the user does not set up the truncation boundary far enough for the specific structure under analysis and level of accuracy demanded.

Acknowledgment

This work was supported in part by the International S&T Cooperation Program under Grant 2016YFE0121600, in part by the China Postdoctoral Science Foundation under Grant 2017M613068, in part by the National Key Research and Development Program of China under Grant 2017YFB0202102 and in part by the Special Program for Applied Research on Super Computation of the NSFC-Guangdong Joint Fund under Grant No.U1501501. The authors would also like to thank the support of the Ministerio de Educación y Ciencia, Spain, under Projects TEC2016-80386-P and CAM S2013/ICE-3004.

References

[1] R. F. Harrington, "Boundary integral formulations for homogenous material bodies," *Journal of Electromagnetic Waves and Applications*, vol. 3, no. 1, pp. 1–15, 1989.

[2] Y. Zhang and T. K. Sarkar, *Parallel Solution of Integral Equation Based EM Problems in the Frequency Domain*. Wiley-IEEE Press, Jul. 2009.

[3] J. M. Jin, *The Finite Element Method in Electromagnetics*. John Wiley & Sons, Inc., 1993.

[4] M. Salazar-Palma, T. K. Sarkar, L. E. García-Castillo, T. Roy, and A. R. Djordjevic, *Iterative and Self-Adaptive Finite-Elements in Electromagnetic Modeling*. Norwood, MA: Artech House Publishers, Inc., 1998.

[5] W. C. Chew, J. M. Jin, E. Michielssen, and J. M. Song, Eds., *Fast and Efficient Algorithms in Computational Electromagnetics*. Artech House Publishers, Inc., 2001.

[6] E. Suter and J. R. Mosig, "A subdomain multilevel approach for the efficient MoM analysis of large planar antennas," *Microwave and Optical Technology Letters*, vol. 26, pp. 270–277, 2003.

[7] J. Yeo, V. Prakash, and R. Mittra, "Efficient analysis of a class of microstrip antennas using the characteristic basis function method (CBFM)," *Microwave and Optical Technology Letters*, vol. 39, no. 6, pp. 456–464, Dec. 2003.

[8] J. M. Jin and D. J. Ryley, *Finite Element Analysis of Antennas and Arrays*. Wiley-IEEE Press, 2009.

[9] R. Fernández-Recio, L. E. Garcia-Castillo, I. Gómez-Revuelto, and M. Salazar-Palma, "Convergence study of a non-standard Schwarz domain decomposition method for finite element mesh truncation in electromagnetics," *Progress In Electromagnetics Research (PIER)*, vol. 120, pp. 439–457, 2011.

[10] I. Gómez-Revuelto, L. E. García-Castillo, and L. F. Demkowicz, "A comparison between PML, infinite elements and an iterative BEM as mesh truncation methods for *hp* self-adaptive procedures in electromagnetics," *Progress In Electromagnetics Research (PIER)*, vol. 126, pp. 499–519, 2012.

[11] L. E. García-Castillo, I. Gómez-Revuelto, F. Sáez de Adana, and M. Salazar-Palma, "A finite element method for the analysis of radiation and scattering of electromagnetic waves on complex environments," *Computer Methods in Applied Mechanics and Engineering*, vol. 194/2-5, pp. 637–655, Feb. 2005.

[12] I. Gómez-Revuelto, L. E. García-Castillo, M. Salazar-Palma, and T. K. Sarkar, "Fully coupled hybrid method FEM/high-frequency technique for the analysis of radiation and scattering problems," *Microwave and Optical Technology Letters*, vol. 47, no. 2, pp. 104–107, Oct. 2005.

[13] J. P. Berenger, "A perfectly matched layer for the absorption of electromagnetic waves," *Journal of Computational Physics*, vol. 114, pp. 185–200, Oct. 1994.

[14] R. Fernández-Recio, L. E. García-Castillo, I. Gómez-Revuelto, and M. Salazar-Palma, "Fully coupled hybrid FEM-UTD method using NURBS for the analysis of radiation problems," *IEEE Transactions on Antennas and Propagation*, vol. 56, no. 3, pp. 774–783, Mar. 2008.

[15] S. Alfonzetti, G. Borzi, and N. Salerno, "Iteratively-improved Robin boundary conditions for the finite element solution of scattering problems in unbounded domains," *International Journal for Numerical Methods in Engineering*, vol. 42, pp. 601–629, 1998.

[16] M. N. Vouvakis, K. Zhao, S. M. Seo, and J.-F. Lee, "A domain decomposition approach for non-conformal couplings between finite and boundary elements for unbounded electromagnetic problems in R^3," *Journal of Computational Physics*, vol. 225, no. 1, pp. 975–994, 2007, doi:10.1016/j.jcp.2007.01.014.

[17] D. Garcia-Donoro, L. E. Garcia-Castillo, and S. W. Ting, "Verification process of finite-element method code for electromagnetics: Using the method of manufactured solutions." *IEEE Antennas and Propagation Magazine*, vol. 58, no. 2, pp. 28–38, April 2016.

[18] J. C. Nédélec, "Mixed finite elements in R^3," *Numerische Mathematik*, vol. 35, pp. 315–341, 1980.

[19] L. E. García-Castillo and M. Salazar-Palma, "Second-order Nédélec tetrahedral element for computational electromagnetics," *International Journal of Numerical Modelling: Electronic Networks, Devices and Fields (John Wiley & Sons, Inc.)*, vol. 13, no. 2-3, pp. 261–287, March-June 2000.

[20] L. E. García-Castillo, A. J. Ruiz-Genovés, I. Gómez-Revuelto, M. Salazar-Palma, and T. K. Sarkar, "Third-order Nédélec curl-conforming finite element," *IEEE Transactions on Magnetics*, vol. 38, no. 5, pp. 2370–2372, Sep. 2002.

[21] A. Amor, L. Emilio Garcia-Castillo, and D. García Doñoro, "Second-order nédélec curl-conforming prismatic element for computational electromagnetics," vol. 64, pp. 1–1, 10 2016.

[22] M. Abramowitz and I. A. Stegun, *Handbook of Mathematical Functions*. New York: Dover, 1965.

[23] D. Sanks, "Non-linear transformations of divergent and slowly-convergent sequences," *Journal of Mathematical Physics*, no. 34, pp. 1–42, 1955.

[24] P. P. Ewald, "Dispersion und doppelbrechung von Elecktronengittern (Kristallen)," dissertation, München, 1912, also *Ann. Phys.* 49, p.1, 1916.

[25] ——, "Die Berechnung optischer und elektrostatischer Gitterpotentiale," *Ann. Phys.*, no. 64, pp. 253–287, 1921.

[26] N. Kinayman and M. I. Aksun, "Comparative study of acceleration techniques for integral and series in electromagnetic problems," *Radio Science*, no. 30, pp. 1713–1722, 1995.

[27] K. E. Jordan, "An efficient numerical evaluation of the Green's function for the Helmholtz operator on periodic structures," *Journal of computational physics*, no. 63, pp. 222–235, 1986.

[28] D. R. W. Thomas F. Eibert, John L. Volakis and D. R. Jackson, "Hybrid FE/BI modeling of 3-D doubly periodic structures utilizing triangular prismatic elements and an MPIE formulation accelerated by the ewald transformation," *IEEE Transaction on Antennas and Propagation*, no. 47, pp. 843–850, may 1999.

[29] J.-M. Jin, Z. Lou, Y.-J. Li, N. Riley, and D. Riley, "Finite element analysis of complex antennas and arrays," *IEEE Transaction on Antennas and Propagation*, vol. 56, no. 8, pp. 2222–2240, Aug 2008.

[30] Y. Zhang, T. K. Sarkar, X. Zhao, D. Garcia-Donoro, W. Zhao, M. Salazar, and S. Ting, *Higher Order Basis Based Integral Equation Solver (HOBBIES)*. John Wiley & Sons, Inc., 2012, iSBN: 9781118140659.

[31] X. Li, L. Lei, H. Zhao, L. Guo, M. Jiang, Q. Cai, Z. Nie, and J. Hu, "Efficient solution of scattering from composite planar thin dielectric-conductor objects by volume-surface integral equation and simplified prism vector basis functions," *IEEE Transactions on Antennas and Propagation*, pp. 1–1, 2018.
[32] W. Luo, S. Yang, and Z. Nie, "A wideband and dual polarization base station antenna for imt-advanced system," in *Proceedings of 2011 Cross Strait Quad-Regional Radio Science and Wireless Technology Conference*, vol. 1, July 2011, pp. 483–486.
[33] "HFSS," http://www.ansys.com/.